JOURNAL OF SPACECRAFT AND ROCKETS
Vol. 37, No. 6, November–December 2000

Hybrid Euler/Direct Simulation Monte Carlo Calculation of Unsteady Slit Flow

Roberto Roveda,* David B. Goldstein,† and Philip L. Varghese‡
University of Texas at Austin, Austin, Texas 78712-1085

An adaptive computational technique that couples an adaptive discrete velocity method with the direct simulation Monte Carlo method has been used to analyze the unsteady evolution of a jet issuing from a slit subject to a pressure differential. This work is motivated by the need to study thruster plume impingement on spacecraft. The method adaptively decomposes the domain according to the degree of local translational nonequilibrium that is quantified by appropriate breakdown parameters. Disconnected patches that employ the direct simulation Monte Carlo solution deform adaptively to track nonequilibrium regions of the flow. The approach allows one to resolve complicated transient flow structures through the concentration of a large number of simulated particles in non-equilibrium regions. Simulations of the jet show that a weak shock wave initially propagates into the flow followed by the high-density jet core. The flow accelerates through an expansion region bounded by two shear layers that form a characteristic barrel structure. The behavior of the flow is investigated as the jet strikes a target plate.

Nomenclature

a	=	speed of sound, $\sqrt{(\gamma P/\rho)}$, m/s
$\bar{c}$	=	average molecular speed, $\sqrt{(8kT/\pi m)}$, m/s
h	=	height, m
Kn_{GLL}	=	gradient-length local Knudsen number
Kn_s	=	slit Knudsen number, λ_1/h_s
k	=	Boltzmann's constant, 1.38×10^{-23} J/K
m	=	molecular mass, kg
$\dot{m}$	=	mass flow rate (flux) through slit, kg/(m^2 s)
N_g	=	number of direct simulation Monte Carlo (DSMC) ghost levels in a cell
n	=	number density (real molecules/m^3)
P	=	thermodynamic pressure, Pa
P_B	=	Bird's breakdown parameter
P_{12}	=	reservoir initial pressure ratio, P_1/P_2
Re_s	=	slit Reynolds number, $\rho_1 a_1 h_s/\mu_1$
T	=	thermodynamic temperature, K
t	=	time, s
U	=	macroscopic velocity component in x direction, m/s
V	=	macroscopic velocity component in y direction, m/s
v_{rel}	=	DSMC collision relative velocity, m/s
γ	=	ratio of specific heats
λ	=	mean free path, m
λ_{xy}	=	mean free path at location x, y, m
ν	=	DSMC collision frequency (number of real collisions/s)
ρ	=	macroscopic density, kg/m^3
ρ_N	=	normalized density gradient
σ	=	variable hard sphere collision cross section dependent on DSMC collision relative velocity, $\sigma(v_{\mathrm{rel}})$, m^2
ω	=	temperature exponent for viscosity coefficient

Subscripts

s	=	slit
x, y	=	Cartesian coordinate axes, location x, y
w	=	wall
1, 2	=	high-, low-pressure reservoir

Received 6 December 1999; revision received 4 May 2000; accepted for publication 16 May 2000.

*Graduate Research Assistant, Department of Aerospace Engineering and Engineering Mechanics; currently Senior CAD Engineer, Intel Corp., SC12-205 M4, 2200 Mission College Boulevard, Santa Clara, CA 95052; roberto.roveda@intel.com.

†Associate Professor, Department of Aerospace Engineering and Engineering Mechanics; david@cfdlab.ae.utexas.edu. Senior Member AIAA.

‡Professor, Department of Aerospace Engineering and Engineering Mechanics; varghese@mail.utexas.edu. Senior Member AIAA.

Introduction

IT is well known that integration methods for the Euler equations[1,2] and particle-based methods [direct simulation Monte Carlo (DSMC[3,4])] are often inadequate to model complex near-continuum flows when applied separately. The Euler equations are strictly confined to the solution of equilibrium flows, whereas the Navier–Stokes (NS) equations can only describe first-order variations from the near-equilibrium state due to mass, momentum, and thermal diffusion. The DSMC approach is equally valid in all regimes, but becomes more computationally expensive as the flow progresses from free molecular, through transitional, to continuum. Recently, hybrid schemes that combine the efficiency of the Euler or the NS equation solvers in the continuum region with the accuracy of the DSMC method in nonequilibrium flow areas have received increasing attention.[5–10]

The purpose of the present paper is to apply a hybrid adaptive discrete velocity (ADV)–DSMC[11–13] method to the two-dimensional, unsteady analysis of pressure driven slit flow, which is expected to contain continuum, transitional and rarefied flow regions simultaneously. In the simulation, the flow exhausts from a high-pressure reservoir (reservoir 1) into a low-pressure chamber (reservoir 2) through a slit whose width measures $28\lambda_1$. For a given slit configuration, a wide range of conditions may be obtained by varying the pressure ratio P_{12} and the slit Knudsen number Kn_s (or equivalently, the slit Reynolds number Re_s). For example, in orifice flow a viscous-dominated Stokes flow arises at nearly isobaric initial conditions, whereas a compressible freejet should appear at large P_{12} (Ref. 14). Initial conditions in reservoir 1 for the present calculations yield $Kn_s = 0.035$ and $P_{12} = 10$. By the adopting of such a pressure ratio, choked flow is expected near the throat, and a supersonic jet develops downstream of the slit. A small target plate is positioned in reservoir 2, approximately seven slit heights downstream from the slit.

The present simulation addresses a number of questions of interest to the physics, numerical analysis, and engineering communities. From the physics standpoint, it is interesting to resolve the jet structure during its development and as it strikes the target plate. Numerically, the simulation provides the opportunity to test the validity of the interface between ADV and DSMC in two-dimensional calculations and of the adaptive regridding procedure. Finally, the simulation constitutes a basic step toward the accurate numerical analysis of thruster plume flows impinging on spacecraft surfaces

such as solar panels. In this engineering context, the simulation furthers the effort to determine unsteady loads on a target exposed to a freejet plume.[9,15]

Literature Review

We briefly summarize early studies of orifice and slit flows that concentrated on the theoretical evaluation of mass flow rate throughout the continuum, transitional, and rarefied regime. Liepmann[14] explains the attainable flow conditions as a function of appropriately defined Reynolds and Mach numbers (a formulation equivalent to the Knudsen number through $Kn \approx$ Mach number/Reynolds number) and presents experimental results for the mass flow rate at large pressure ratios. Willis[16] presents the theoretical solution for free molecular orifice and slit flow by applying an iterative method to the integral form of the Boltzmann equation. Stewart[17] uses Willis's[16] iterative method for the Bhatnagar–Gross–Krook (BGK) form of the Boltzmann equation to correct the infinite pressure ratio mass flow rate in a nearly free molecular flow for the effect of finite pressures.

Wadsworth and Erwin[18,19] published a series of results on pressure-driven, subsonic flow through a slit to compare solutions from pure DSMC and from pure NS calculations. Of particular relevance to the current method is their application of a hybrid continuum/particle approach[6] to the analysis of slit flow. In the hybrid NS–DSMC calculation, the authors employed a cell-centered, flux-matching interface formulation. In the technique, the cumulative sampled value of DSMC cell-centered conserved quantities adjacent to the interface provided the boundary condition to integrate the NS equations in the continuum region. The flux into the DSMC region was calculated by interpolation to the interface of the cell-centered NS solution. Thus, the coupling was not time accurate but improved as steady-state conditions were approached. The hybrid simulation of Wadsworth and Erwin achieved a speedup by a factor of about two over the full DSMC calculation. A strongly coupled hybrid method has not previously been applied to the study of supersonic flow from a slit, to unsteady two-dimensional flows, or to plume impingement problems.

Present Approach: Summary

The numerical procedure employed in the unsteady simulation of slit flow is a hybrid Euler–DSMC solver.[11–13] Nadiga's ADV[20,21] method, the Euler approach used in this hybrid scheme, is a kinetic theory approach that integrates the Euler equations for a 27 discrete velocity (four speed) gas model through the use of a flux-splitting/total variation diminishing scheme based on Nadiga and Pullin's flux-splitting equilibrium method.[22] The ADV approach assumes an equilibrium distribution function based on macroscopic properties at each cell center but retains a nonequilibrium distribution function at cell boundaries because of the superposition of distinct cell-centered fluxes from neighboring cells. For nonequilibrium flows, DSMC[3,4] is a well-established, extensively tested solver that extracts the macroscopic properties by simulating the microscopic structure of the flow with an ensemble of simulated molecules. The simulated molecules undergo a cycle of separate move and collide phases. Macroscopic properties are periodically sampled by calculating moments of the particle's distribution function within each cell of a sampling grid.

In its current implementation, DSMC adapts the free-cell collision procedure[13,23,24] to increase the accuracy of the method and simultaneously to allow sampling cells whose dimensions may be greater than the local mean free path. The free-cell approach describes the expansion and contraction of the DSMC collision partner selection regions in relation to the flow gradients. The method selects a particle-centered equilateral interaction region whose size is related to the density-based gradient local Knudsen number. The width of this variable sized, particle-centered free cell is

$$d_{\text{interact}} = \Delta x \cdot \left[f_1 + f_2 \cdot \left(1 - \frac{Kn_{\text{GLL}}}{Kn_{\text{GLL-max}}} \right) \right] \qquad (1)$$

where f_1 and f_2 are arbitrary, problem-dependent constants such that $f_1 + f_2 = 1$ and $Kn_{\text{GLL-max}}$ is the maximum local Knudsen number in the computational domain. Collisions are rejected without bias if particles are spaced greater than d_{interact}. Through Eq. (1), the collision partner selection distance in near-equilibrium regions coincides with background (property sampling) cells, whereas the particle distance in nonequilibrium regions varies with the property gradients.

The hybrid technique decouples the calculation into separate but interacting ADV and DSMC steps. Between the two regions is an interface. In the continuum region, the ADV Euler solver determines the interface continuum fluxes through the use of DSMC macroscopic properties in two overlapping buffer cells, whose noise has been considerably decreased by the application of smoothing ghost cells.[11] The buffer DSMC cells adjacent to the interface are treated as an extension of the ADV domain, and the macroscopic DSMC properties therein are used to obtain interface fluxes necessary for finite volume integration. In the opposite direction, particles travel into the DSMC domain from a layer of two ADV cells disguised as particle reservoir cells. Cell-centered ADV density values in the reservoir cells determine the number of reservoir DSMC particles to initialize. For each reservoir cell, particle velocities are drawn from the Maxwell–Boltzmann velocity distribution function that reflects the reservoir cell properties. Particles are then randomly positioned within the cell and moved according to the appropriate time step. Particles that do not enter the DSMC domain are destroyed.

DSMC provides ADV with property values whose root-mean-square noise is proportional to the inverse square root of the number of simulated DSMC particles that generate the values. The application of ghost cells containing cloned particles provides a localized increase in the number of particles (and therefore smoothing) near the interface without excessive computational cost. An N_g-parallel DSMC move-collide cycle occurs in a frame of N_g overlapping DSMC ghost levels that surround each DSMC patch and interact with ADV. The ensemble average of the N_g relatively independent solutions yields smoother ADV boundary conditions than those that would be obtained with a single DSMC level. For example, we may compute with an average of 40 particles per cell in most of a DSMC region, whereas, with three levels of ghost cells ($N_g = 3$) near the interface, the ADV buffer cells see a random noise level closer to that found with 160 (three ghost levels plus one real level) particles per cell. For more detailed information about the method, the reader is referred to Refs. 11–13.

Adaptive Regridding Procedure

The hybrid technique[11–13] has been upgraded to adaptively position the interface between DSMC and the continuum domains into a region of mutual validity where the effect of mass diffusion, viscosity, and heat conduction are negligible. The automatic processes of interface positioning can occur at every time step. The present hybrid method places the interface conservatively because the technique employs an Euler solver instead of a NS solver and because of the uncertainty associated with the high noise levels (even after the application of ghost levels) accompanying unsteady computations. We first summarize how the interface location is determined and then describe how the switch in each cell is made between the two methods.

Low-Pass Filter for Property Field

A moving average, low-pass filter similar to that employed in Refs. 11–13 was adapted for use in the analysis of two-dimensional flows. Filtered property values are only used to determine where to place the ADV and DSMC regions. Tiles composed of cells surrounding the cell of interest contribute to the average of the properties in the center cell. For example, the following calculations employ square smoothing tiles whose sides measure 5 cells so that 25 cells (1 at the center and the 24 surrounding) contribute to the average in the center cell. If the moving average requires information outside the computational boundary, properties from the last cell adjacent to the boundary are copied (extrapolated) to fictitious cells. The low-pass filter smears the property gradients to differing degrees depending on the number of passes. Hence, the resulting inflated nonequilibrium region is an added safeguard against the incorrect application of the Euler solver.

Evaluation of the Cutoff Parameters

The gradient local Knudsen number[3,25] Kn_{GLL} and Bird's parameter[26] P_B embody the physical and numerical criteria that are used to identify the boundary between continuum and rarefied computational domains.

The gradient local Knudsen number (presented here in two-dimensional, steady form),

$$Kn_{\mathrm{GLL}} = \frac{\lambda_{xy}}{\rho}\sqrt{\left(\frac{\partial\rho}{\partial x}\right)^2 + \left(\frac{\partial\rho}{\partial y}\right)^2} \tag{2}$$

based on the local density gradient, predicts the breakdown of continuum approaches in local nonequilibrium flow regions. Similarly, Bird's study of expanding flows indicates failure of the continuum approach because P_B [Eq. (3)] increases above the range 0.02–0.05 in the direction of the flow streamlines.[26] The present calculations employ a variation of P_B that evaluates the density gradients in the Cartesian directions instead of along a streamline:

$$P_B = \frac{1}{\nu}\left|\frac{U}{\rho}\frac{\partial\rho}{\partial x} + \frac{V}{\rho}\frac{\partial\rho}{\partial y}\right| \tag{3}$$

We also employ a normalized density gradient,

$$\rho_N = \frac{\lambda_1}{\rho}|\nabla\rho| = \frac{\lambda_1}{\rho}\sqrt{\left(\frac{\partial\rho}{\partial x}\right)^2 + \left(\frac{\partial\rho}{\partial y}\right)^2} \tag{4}$$

that has been found to detect the leading temperature shock better than Kn_{GLL} does for one-dimensional shock waves.

The moving average procedure provides a smoothed density and velocity field, which in turn yield Kn_{GLL} [Eq. (2)], P_B [Eq. (3)], and ρ_N [Eq. (4)]. Central differencing is used to evaluate the derivatives. Selecting appropriate values of the cutoff parameters is a delicate art: values that are excessively small resolve unwanted statistical noise, whereas values that are excessively large allow the incorrect application of the Euler solver in nonequilibrium areas. The values of the cutoff parameters used in this simulation are provided in the "Results" section.

Placement of DSMC Patches

The current technique reshapes and repositions DSMC patches periodically to track high gradient, unsteady phenomena such as shocks, expansions, shear waves, and boundary layers. In the adaptive calculations that follow, a regridding interval of five time steps proved suitable to track unsteady wave patterns in the jet structure.

Roveda et al.[11,12] explain how overlapping ASCII maps detail the multiple characteristics of a cell within regridding steps. For example, an ADV cell may also be a reservoir DSMC cell, and a DSMC cell may simultaneously be a ghost cell and a buffer cell that provides boundary conditions for ADV. The rebuilding of a new set of ASCII maps that describe the cells proceeds as follows. The properties in the center cell of smoothing tiles, that is, 5×5 sampling cells, are considered representative of the tile. The regridding procedure uses Knudsen number Kn_{GLL}, P_B, and ρ_N cutoff values in the representative cell to determine whether all cells in the tile change their character from ADV to DSMC or vice versa. At first only pure ADV and pure DSMC tiles are identified.

Next, coarse and fine smoothing procedures eliminate spurious, miniscule patches of DSMC or ADV embedded within each other. To identify the boundary between DSMC and ADV regions, the procedure separately sweeps the grid at the tile interval in the vertical and horizontal directions. For each tile, the algorithm determines the nature of the eight surrounding tiles (corresponding to the eight cardinal points). If five or more of the surrounding tiles bear a character (ADV or DSMC) opposite to that of the tile under consideration, the current tile is converted to that character, otherwise it is left unchanged. The smoothing procedure is repeated at the cell level. This neighbor survey approach resembles a localized annealing procedure that leads to reasonably smooth regions of DSMC and ADV.

The subsequent steps consist of exchanging information between microscopic and macroscopic descriptions for cells that change character. If a tile is to switch from real or ghost DSMC to ADV, sampling the DSMC particles from corresponding cells generates ADV macroscopic properties for each cell in the tile. All ghost and pure DSMC particles in the tile's cells are then removed from the DSMC array. Conversely, if the switch from ADV to DSMC occurs, DSMC particles are initialized from the ADV macroscopic properties and randomly positioned within the new DSMC cells in the tile. A further sweep at the cell level re-identifies the DSMC–ADV interface and changes the character of boundary cells to create the appropriate frame of ghost cells, reservoir DSMC cells, and ADV buffer cells. The algorithm assigns ghost cells according to a predetermined depth. Turning regular DSMC to ghost DSMC cells requires cloning the regular cells through the required N_g ghost levels.

Results

The adaptive, hybrid ADV–DSMC technique has been applied to analyze pressure-driven slit flow. This case explores the supersonic jet structure as it evolves from the initial burst of the numerical diaphragm through the jet impingement on a target plate situated downstream from the slit. Figure 1 shows the relevant initial and boundary conditions of the simulation, whereas Fig. 2 outlines the dimensions (Table 1) that characterize the domain.

Relevant Simulation Parameters

In this simulation reservoir 1 is initialized to a density of 1.785×10^{-4} kg/m^3 and a temperature of 500 K. To create a starting pressure ratio of $P = 10$, we initialize each of the DSMC cells to the left of the slit with 100 simulated molecules and those to the right with 1000 molecules. Variable hard sphere diatomic (two rotational degrees of freedom) DSMC particles ($\omega = 0.74$) have the mass of nitrogen molecules. Simulated DSMC molecules are initialized according to the respective reservoir macroscopic properties, and the flow evolves in an unsteady manner from an initial state of rest. Solutions are advanced with time steps measuring about $\frac{1}{10}$th of the equilibrium collision time in reservoir 1, and the macroscopic properties are extracted every 40 time steps. The values of the free-cell parameters

Table 1 Relevant dimensions for the flow simulation in various units

Distance	Cells	λ_1	Slit heights	Meters
h_{AB}	5	5.097	0.178	0.020
h_{BD}	12	12.233	0.429	0.048
h_{KL}	5	5.097	0.178	0.020
$h_{\mathrm{HI}} = h_{\mathrm{LM}}$	114	116.220	4.071	0.456
h_{IL}	28	28.545	1.000	0.112
h_{CU}	198	201.856	7.071	0.792
h_{TF}	100	101.948	3.571	0.400
h_{MR}	142	144.766	5.071	0.568

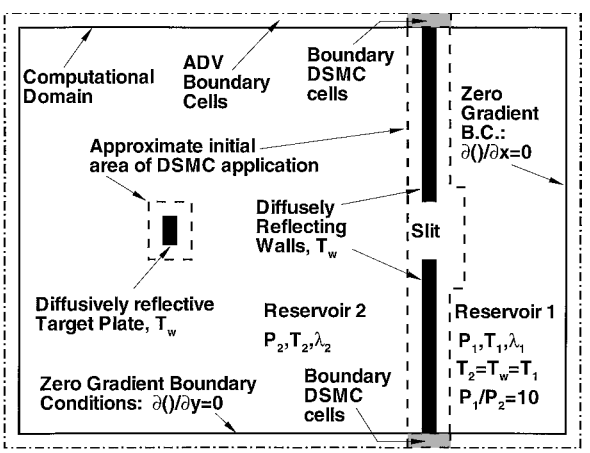

Fig. 1 Computational domain for adaptive, hybrid simulation of pressure driven slit flow.

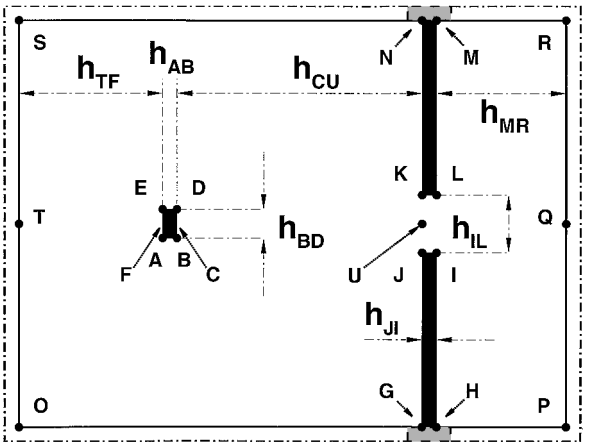

Fig. 2 Relevant distances in computational domain.

are set to $f_1 = 0.2$ and $f_2 = 0.8$, respectively. The simulations were run on a 500-MHz Pentium II processor and used about 450 MB of storage when the total (real plus ghost) number of particles peaked at a maximum value of about 14×10^6. Each computational time step represents 0.5 μs of simulated real time. A typical simulation of 12,000 time steps requires about 50 h of computational time on a single Pentium II processor workstation.

The initial layout of the calculations is similar to that adopted for the fixed patch, two-dimensional hybrid calculation of Refs. 11 and 12. The computational domain (OPRSO in Fig. 2) measures 444×250 cells and initially consists of 6217 DSMC cells (4551 pure DSMC cells and 1666 ghost DSMC cells) and 104,783 ADV cells. The grid employs equisized ADV and DSMC cells, each of which measures $1.02\lambda_1$ on the side. Note that, even if the dimension of the sampling cells is of the order of the local mean free path, accuracy is determined more directly by the size of the collisional free cells. In the highly nonequilibrium regions, the free-cell procedure (with $f_1 = 0.2$) selects a collision partner distance of approximately $\frac{1}{5}\lambda_1$. The vertical solid walls that flank the slit are diffuse scatterers at a temperature of 500 K. The simulation has a slit Reynolds number Re_s of approximately 420.

The dashed lines in Fig. 1 delineate the approximate location of the initial DSMC patches that contain the slit vertical walls and the target plate. Each DSMC patch consists of real DSMC cells in the interior and a five-cell-wide frame of ghost cells five levels deep (one real level plus five ghost levels). Subsequent adaptive DSMC patches evolve from the initial layout. The ghost region that surrounds the variable DSMC domain maintains the width (of five) and depth (of five). In the current calculation, repositioning of the DSMC patches occurs every five time steps.

The dash–dot line in Figs. 1 and 2 denotes a permanent, three-cell-deep layer of ADV cells adjacent to the computational boundary to provide zero gradient boundary conditions there. The forced application of ADV prevents DSMC cells from being positioned adjacent to the boundaries except for boundary DSMC cells (points N, M, G, and H in Fig. 2) present in the initial DSMC patch that surrounds the slit walls. The implementation of the boundary conditions at the corners formed by the slit wall and the top and bottom boundaries requires particular care because both the wall diffuse reflection and the zero gradient boundary condition must be modeled correctly. The current approach copies particles within the last DSMC cell inside and adjacent to the computational boundary to fictitious cells outside the computational boundary. These fictitious cells function thereafter as reservoir cells. Otherwise, DSMC cells within the computational boundary interact normally with their ADV neighbors.

The majority of reservoir 1 is modeled with ADV throughout the computation except for permanent DSMC regions adjacent to the slit walls and in the region that surrounds the slit itself. No new DSMC patches are positioned in the high-pressure reservoir during the regridding process. This treatment is justified because nearly uniform, equilibrium conditions prevail in reservoir 1 with the exception of the weak initial, propagating expansion wave. Also, the computational cost associated with the DSMC modeling of the whole high-density regions justifies the application of the continuum solver there. In view of the computational cost, DSMC is judiciously applied in the high-pressure region only to resolve the boundary layer that develops near solid surfaces and any high gradients that occur near the slit. Within reservoir 1, the ADV–DSMC interface adequately simulates subsonic inflow/outflow conditions at the right interface of the fixed DSMC patch that envelops the slit.

Cutoff Parameters

Figures 3–5 show instantaneous realizations of each of the three cutoff parameter values [Eqs. (2–4)] for the slit flow simulation after 1440 time steps ($\Delta t = 1/10\nu_1 \sim 0.638$ μs). The threshold value of the breakdown parameters in this simulation differ from the generally accepted breakdown thresholds presented in the literature [$Kn_{GLL} \sim 0.05-0.1$ (Refs. 3 and 25) and $P_B \sim 0.02-0.05$ (Refs. 3 and 26)] because of the smoothing procedure that is applied to the unsteady, statistically noisy property signal. Smoothing must be applied because, unlike steady flows, it is not possible to time average at a fixed location in the computational domain. Because of large

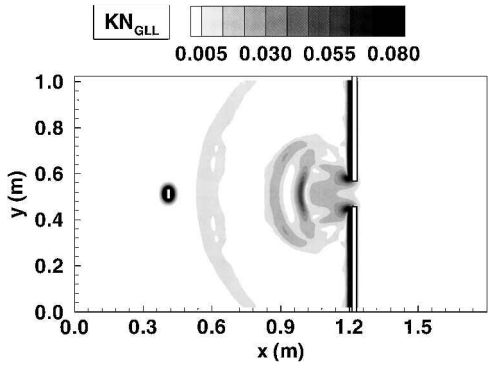

Fig. 3 Gradient local Knudsen number; $t \sim 919\,\theta$s.

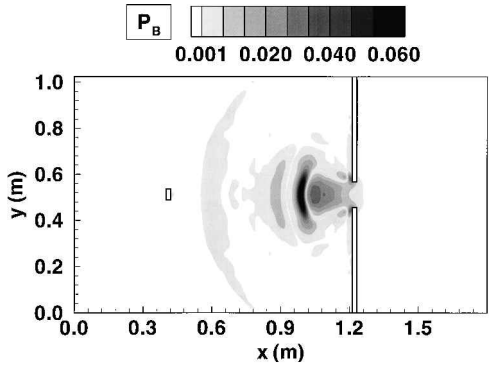

Fig. 4 Bird's parameter[26]; $t \sim 919\,\theta$s.

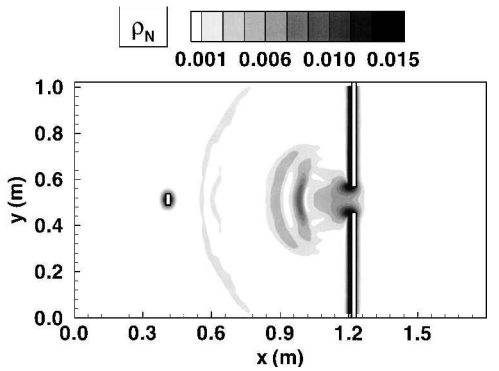

Fig. 5 Normalized density gradient; $t \sim 919\,\theta$s.

smoothing blocks (5 ×5 tiles = 25 cells), the smoothing procedure increases the width of the property gradient and decreases its magnitude. Therefore, the threshold values that result from the smoothed macroscopic property signal identify inflated regions of nonequilibrium around strong gradients. The cutoff values are chosen to capture the weak shock ahead of the jet structure that originates after the rupture of the diaphragm. The current simulation uses the following cutoff values: $Kn_{GLL} = 0.015$, $\rho_N = 0.01$, and $P_B = 0.004$.

Figure 3 shows that the weak starting shock has reached about 0.6 m from the slit; ρ_N and P_B clearly also capture the expansion region and the outline of the plume core. The large values of Knudsen number Kn_{GLL} and ρ_N adjacent the slit walls and the target plate occur for three reasons. First, the smoothing of the property signal is carried out in patches of 5 ×5 (25 cells), and hence, no smoothing is carried out in a three-cell layer adjacent to the slit walls. Second, the calculation of the absolute value of a statistically noisy DSMC signal always produces an artificially inflated property gradient. This effect is more pronounced for flow at rest. Third, the property gradient is calculated through the solid surface, and the disparity between the initial flow conditions and fixed, dummy values within the solids guarantees a seemingly high-density gradient adjacent to surfaces. The miscalculation of the parameters there does not affect the simulation, however, because a permanent DSMC patch envelops the slit walls anyway.

Flow Structure

Figures 6 and 7 show the density contours and the corresponding placement of DSMC and ADV patches at time $t \sim 1021$ μs. Figures 8–11 show the density contours, the placement of ADV and DSMC patches, selected velocity vectors, and the Mach number contours for $t \sim 1531$ μs. Likewise, Figs. 12 and 13 show the properties corresponding to Figs. 6 and 7 for $t \sim 4084$ μs and Figs. 14–17 show the properties corresponding to Figs. 8–11 for $t \sim 6126$ μs.

At $t \sim 1021\mu$s (Fig. 6) the initial weak shock wave (B1) of strength ~Mach 1.3 propagates toward the target plate. The lag of the vertical DSMC patch relative to the initial weak compression wave indicates that the cutoff thresholds were not small enough for the DSMC patches to bracket such a weak wave. The starting evolution of an expansion region near the lips of the slit (E1 and E2) can be discerned. The simulation seems to encompass adequately

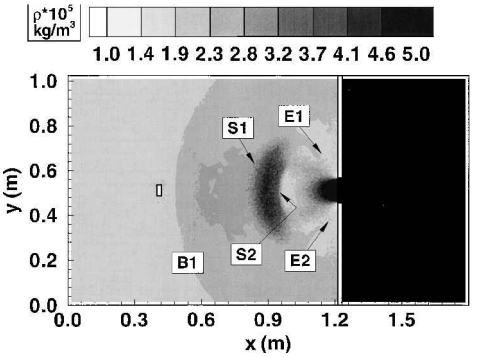

Fig. 6 Density contours; $t \sim 1021\,\theta$s.

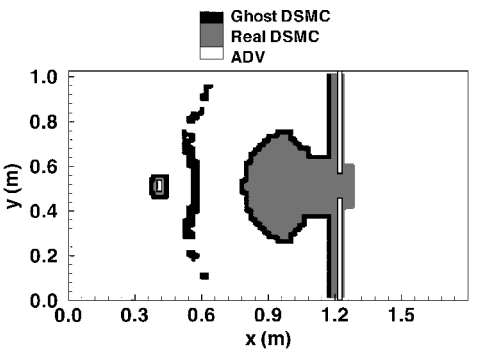

Fig. 7 Placement of ADV and DSMC regions; $t \sim 1021\,\theta$s.

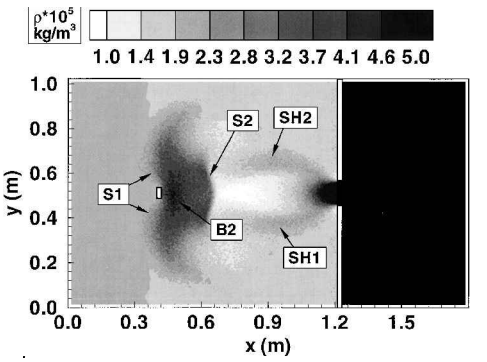

Fig. 8 Density contours; $t \sim 1531\,\theta$s.

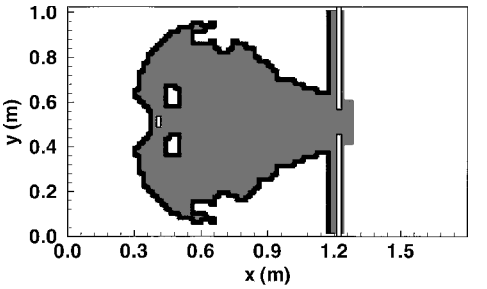

Fig. 9 Placement of ADV and DSMC regions; $t \sim 1531\,\theta$s.

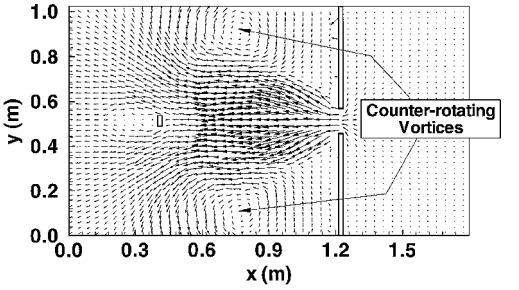

Fig. 10 Selected velocity vectors; $t \sim 1531\,\theta$s.

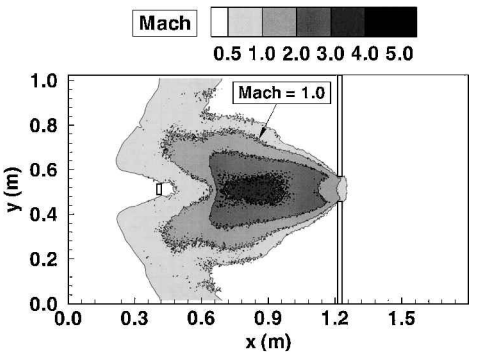

Fig. 11 Mach number contours; $t \sim 1531\,\theta$s.

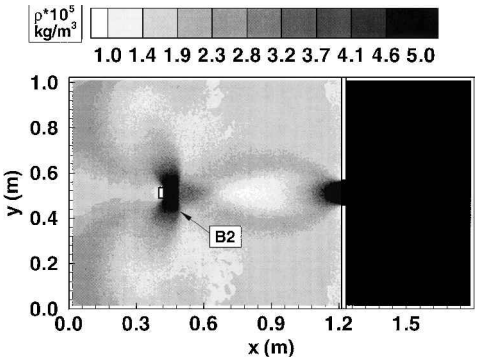

Fig. 12 Density contours; $t \sim 4084\,\theta$s.

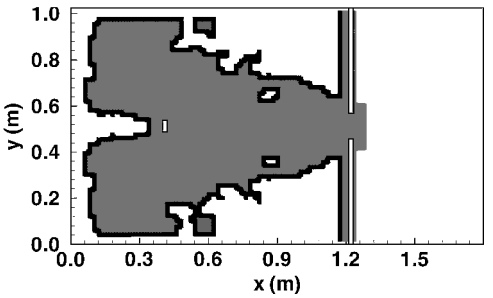

Fig. 13 Placement of ADV and DSMC regions; $t \sim 4084\,\theta$ s.

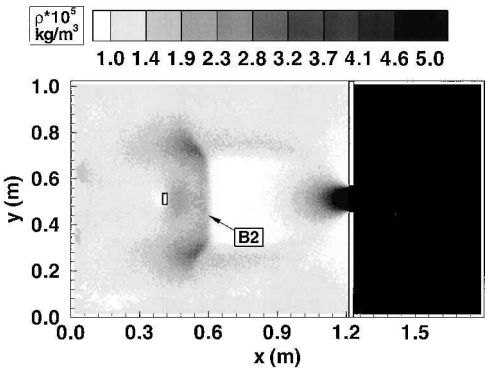

Fig. 14 Density contours; $t \sim 6126\,\theta$ s.

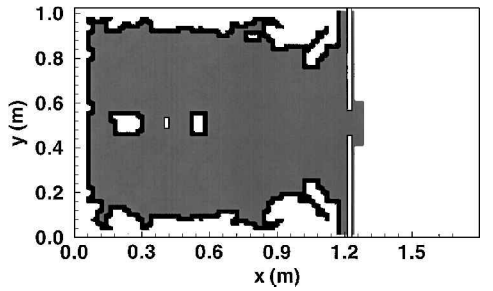

Fig. 15 Placement of ADV and DSMC regions; $t \sim 6126\,\theta$ s.

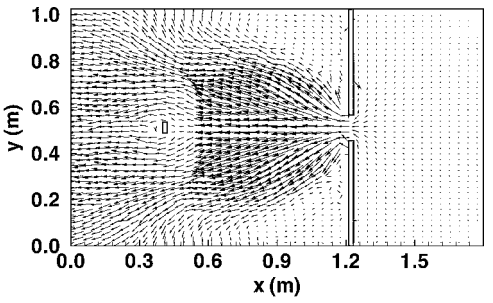

Fig. 16 Selected velocity vectors; $t \sim 6126\,\theta$ s.

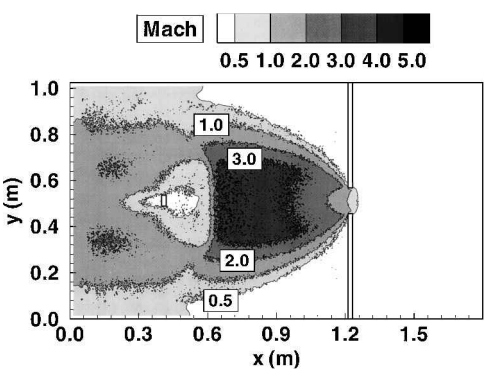

Fig. 17 Mach number contours; $t \sim 6126\,\theta$ s.

the core of the jet structure. The jet front (S1) and normal shock (S2) have separated within the jet core.

By $t \sim 1531\,\mu$s (Fig. 8), wave B1 has exited the domain. A bow shock (B2) develops as the jet front (S1) passes the target plate. The normal shock (S2) continues to travel toward the target plate. The maps in Figs. 7 and 9 clearly show that DSMC computes the whole jet except for two high-pressure central bubbles. The velocity vectors in Fig. 10 show the formation of two counter-rotating startup vortices that convect downstream alongside the jet. The tracking of the vortices with intermittent patches of DSMC in the following frames depends on the threshold values of the cutoff parameters. The lack of complete tracking of these vortices and of the initial weak compression wave with DSMC patches illustrates the difficulty in choosing appropriate threshold values. The simulation must track all of the relevant gradients without overextending the area of DSMC application too far outside nonequilibrium regions. The Mach number contours in Fig. 11 show the rapid expansion and acceleration of the flow downstream of the slit. The shape of the sonic line implies the presence of a barrel-type structure in which high-speed flow is bounded by two shear layers (SH1 and SH2 in Fig. 8). The expansion fan emanating from the slit lip can be discerned. The simulation predicts a curved sonic line at the slit, hence the presence of subsonic flow in the plane of slit.

At time $t \sim 4084\,\mu$s (Fig. 12), one clearly sees a bow shock in front of the target plate. Small vortices are shed from the tip of the target plate, but they are most likely lost due to the viscous flow near the plate. Complicated unsteady flow patterns arise on either side and downstream of the target plate. The shear layers that bound the jet barrel structure are clearly visible. Figure 13 shows that the DSMC region delineates the jet fairly well as the flow continues to expand. However, erratic DSMC patches on either side of the jet may be tracking the two vortices and some of the residual statistical noise present there.

At time $t \sim 6126\,\mu$s (Figs. 14–17), unsteady flow remains present near the plate as the normal shock (B2) retreats toward the slit. The jet remains reasonably symmetric. The velocity vectors in Fig. 16 show the jet flow splitting and turning around the target plate and ending in mixed subsonic/supersonic outflow at the left-hand boundary (OS in Fig. 2) of the computational domain. As expected, flow is entrained into the domain over portions of the top and bottom boundaries just downstream of the slit walls. In addition to the barrel structure similar to that in Fig. 11, the Mach number contours in Fig. 17 show the bow shock at a standoff distance of ~0.18 m upstream of the plate. The plate is immersed in a pocket of subsonic flow.

Figure 18 shows the average density and velocity values of 100 instantaneous slit-plane profiles from $t \sim 3000$ to $6000\,\mu$s. The inset shows the exact position of the slit plane in the computational grid. Note the expected parabolic profile of the density. The velocity is nondimensionalized by the reservoir speed of sound so that it is not to be confused with the local Mach number in the plane of the slit which is nearly sonic. The rapid expansion near the high-density side slit corners (I and L in Fig. 2) accelerates the flow to a higher velocity than that on the centerline. Therefore, the velocity profile in Fig. 18 shows two maxima away from the centerline.

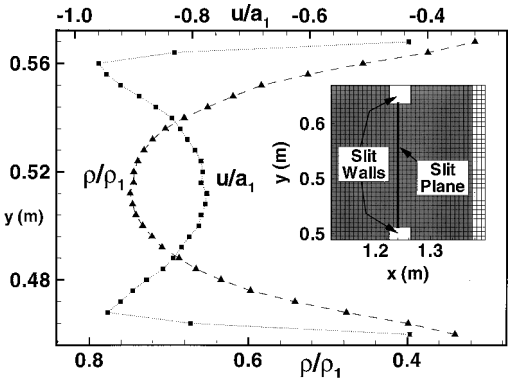

Fig. 18 Average velocity and density profiles at the slit plane.

Table 2 Mass flux

Conditions	$\dot{m}/\rho_1 a_1$
Continuum (γ = 1.4), $[2/(\gamma+1)]^{(\gamma+1)/2(\gamma-1)}$	0.579
Current calculation	0.508
Free molecular, $[1-(1/P_{12})](\bar{c_1}/4a_1)$	0.303

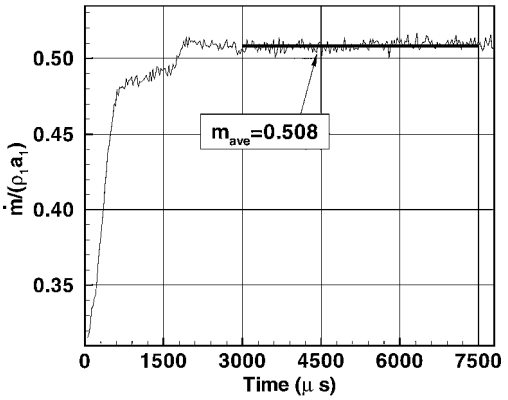

Fig. 19 Mass flow rate through slit.

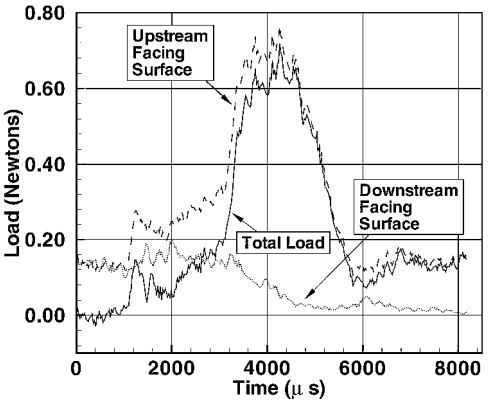

Fig. 20 Transient loads on target plate.

Figure 19 shows the mass flow rate (normalized by $\rho_1 a_1$) obtained by counting the number of DSMC particles crossing the slit in the forward and backward directions. The mass flow rate gradually increases to a constant value that indicates steady (and possibly choked) flow exist in the slit plane. Table 2 compares our results with the steady values predicted by the free molecular and continuum analysis for thin-walled slits. As expected, the value of $\dot{m} = 0.508$ lies between the value predicted by free molecular theory[16] and the continuum value obtained from quasi-one-dimensional compressible flow theory.[27] Our results lie much closer to the continuum solution since $Kn_S = \lambda_1 / h_S \sim 0.0035$.

The transient loads recorded on the target plate (Fig. 20) correspond to expected physical phenomena. Each simulated DSMC particle that diffusively collides on the downstream or upstream vertical facing surfaces contributes $m(\bar{u}_{\text{incoming}} + \bar{u}_{\text{outgoing}})$ to the momentum transferred to the plate. The absolute value of the normal force on the downstream facing plate surface is subtracted from that on the upstream surface to obtain the net load on the plate. The plate rests in quiescent gas until $t \sim 1200\ \mu$s, and as expected, the computed load is zero except for DSMC statistical noise. A substantial increase in the upstream surface load is noted when the compression wave B1 and the jet front S1 strike the plate at $t \sim 1200$ and $3000\ \mu$s, respectively. The force on the downstream surface increases slightly at $t \sim 1200\ \mu$s and subsequently decreases toward zero as low-density conditions develop in the wake.

Figure 21 shows the evolution of the number of real, ghost, and total DSMC particles employed by the simulation during the transient and the quasi-steady-state phase. Several physical events may be identified. The initial increase up to $t \sim 450\ \mu$s in real and ghost

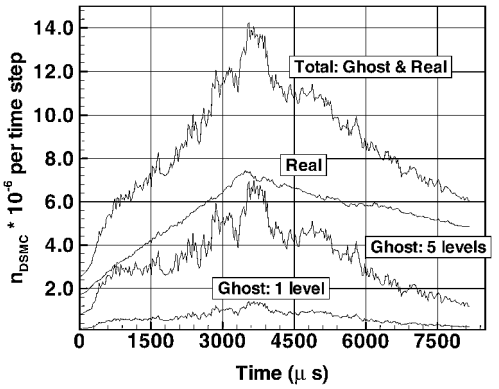

Fig. 21 Evolution of number of DSMC particles during transient phase.

DSMC particles corresponds to the formation of the initial weak shock wave (B1) and the jet leading surface (S1). As it propagates toward the plates, the jet elongates but does not change shape appreciably. A ratio of real to ghost DSMC particles above unity is attained throughout the simulation.

The elongation of the jet from $t \sim 450$ to $2100\ \mu$s causes a linear increase in the number of DSMC particles but only a modest increase in number of ghost DSMC particles. In this particular calculation, the impingement of the jet on the plate ($t \sim 2100\ \mu$s) does not seem to alter the rate of increase of real particles appreciably. The deformation of the DSMC patch that resolves the jet front as it strikes the target plate is responsible for the increase in the number of ghost molecules between $t \sim 2100$ and $3300\ \mu$s. The numbers of real and ghost molecules in the simulation peaks at about 14×10^6 (about 1.6×10^6 per ghost level). Subsequently, the number of ghost particles drops more rapidly than the pure DSMC particles, presumably to approach steady-state values, as the domain becomes filled with real DSMC cells.

Note the large number of molecules devoted to the decrease of statistical noise propagating from the DSMC domain into ADV. The ratio of ghost to real simulated molecules is relatively high in this calculation, and the low ratio of regular DSMC cells to ghost cells obscures the advantage of the ghost procedure over a single-level DSMC calculation with an equivalent number (real plus ghost) of simulated molecules. In a lower Knudsen number calculation, more pronounced savings are expected by using ghost cells while maintaining the same level of statistical noise propagation into the Euler domain. In addition, in three-dimensional flow simulations the proportion of cells at interfaces decreases.

Conclusions

The novel, strongly coupled, hybrid ADV–DSMC adaptive method is applied to the simulation of unsteady pressure driven slit flow. Independent, pliable DSMC patches adequately track flow events during the transient period. The tracking of the initial, weak propagating compression wave and the resolution of the expansion region within a barrel core structure bounded by shear layers constitute interesting features of the expanding slit flow. Mach number contours show a curved sonic line just downstream of the slit. The constancy of the mass flow rate after $t \sim 2400\ \mu$s indicates the presence of steady state and probably choked flow in the slit plane. The behavior of the unsteady load on a target plate has been presented. The present simulation highlights the difficulty of selecting appropriate values of the cutoff parameters that limit the application of the DSMC exclusively within nonequilibrium areas, without tracking statistical noise. DSMC patches resolved the jet consistently early in the simulation but subsequently spread to fill the entire computational domain. In retrospect, different values of the cutoff parameters could have been selected to reduce computational effort. However, the suboptimal regridding procedure does not affect the accuracy and correctness of the results. The current technique is a successful step toward the development of a hybrid numerical tools for rarefied plumes.

Acknowledgments

This work was supported in part by NASA under the University Grant Program (Grant NAG9-804 and NAG9-991). The authors would like to thank the Technical Monitor, F. Lumpkin III, for his assistance and continued support. The authors would like to thank William Barth, Robert McLay, and Benjamin Kirk of the Computational Fluid Dynamics Laboratory and Scott Messec and Reuben Reyes of the Learning Resources Center in the Department of Aerospace Engineering and Engineering Mechanics of the University of Texas at Austin for the technical support provided during the execution of the simulations.

References

[1]Anderson, D., Tannehill, J., and Pletcher, R., *Computational Fluid Mechanics and Heat Transfer*, 1st ed., Hemisphere, New York, 1984, pp. 235–246.

[2]Hirsch, C., *Numerical Computation of Internal and External Flows*, Vol. 2, Wiley, New York, 1988, pp. 132–223.

[3]Bird, G. A., *Molecular Gas Dynamics and the Direct Simulation of Gas Flows*, Clarendon, Oxford, 1994, Chaps. 11–16, pp. 218–407.

[4]Bird, G. A., "Monte-Carlo Simulation in an Engineering Context," *Rarefied Gas Dynamics*, edited by S. S. Fisher, Vol. 74, Pt. 1, Progress in Astronautics and Aeronautics, AIAA, New York, 1981, pp. 239–255.

[5]Wadsworth, D. C., and Erwin, D. A., "One-Dimensional Hybrid Continuum/Particle Simulation Approach for Rarefied Hypersonic Flows," AIAA Paper 90-1690, June 1990.

[6]Wadsworth, D. C., and Erwin, D. A., "Two-Dimensional Hybrid Continuum/Particle Approach for Rarefied Hypersonic Flows," AIAA Paper 92-2975, July 1992.

[7]Hash, D. B., and Hassan, H. A., "A Decoupled DSMC/Navier–Stokes Analysis of Transitional Flow," AIAA Paper 96-0353, Jan. 1996.

[8]Hash, D. B., and Hassan, H. A., "Assessment of Schemes for Coupling Monte Carlo and Navier–Stokes Solution Methods," *Journal of Thermophysics and Heat Transfer*, Vol. 10, No. 2, 1996, pp. 242–249.

[9]Lumpkin, F. E., III, Stuart, P. C., and LeBeau, G. J., "Enhanced Analyses of Plume Impingement During Shuttle–Mir Docking Using a Combined CFD and DSMC Methodology," AIAA Paper 96-1877, June 1996.

[10]Tivari, S., and Klar, A., "An Adaptive Domain Decomposition Procedure for Boltzmann and Euler Equations," *Journal of Computational and Applied Mathematics*, Vol. 90, No. 2, 1998, pp. 223–237.

[11]Roveda, R., Goldstein, D. B., and Varghese, P. L., "A Combined Discrete Velocity/Particle Based Numerical Approach for Continuum/Rarefied Flows," AIAA Paper 97-1006, Jan. 1997.

[12]Roveda, R., Goldstein, D. B., and Varghese, P. L., "Hybrid Euler/Particle Approach for Continuum/Rarefied Flows," *Journal of Spacecraft and Rockets*, Vol. 35, No. 3, 1998, pp. 258–265.

[13]Roveda, R., Goldstein, D. B., and Varghese, P. L., "A Hybrid Euler/DSMC Approach to Unsteady Flows," *Rarefied Gas Dynamics: Proceedings of the 21st International Symposium on Rarefied Gas Dynamics*, edited by R. Brun, R. Campargue, R. Gatignol, and J.-C. Lengrand, Vol. II, Cepadues-Editions, Toulouse, France, 1999, pp. 117–124.

[14]Liepmann, H. W., "Gaskinetics and Gasdynamics of Orifice Flow," *Journal of Fluid Mechanics*, Vol. 10, Pt. 1, 1961, pp. 65–79.

[15]Bouslog, S. A., Fitzgerald, S. M., and Machin, R. A., "Instrument Characterization Tests in a Nitrogen Free Jet," NASA Johnson Space Center, Rept. JSC-26706, March 1995.

[16]Willis, D. R., "Mass Flow Through a Circular Orifice and a Two Dimensional Slit at High Knudsen Numbers," *Journal of Fluid Mechanics*, Vol. 21, No. 1, 1965, pp. 21–31.

[17]Stewart, J. D., "Mass Flow Rate for Nearly-Free Molecular Slit Flow," *Journal of Fluid Mechanics*, Vol. 35, No. 3, 1969, pp. 599–608.

[18]Wadsworth, D. C., and Erwin, D. A., "Numerical Analysis of Rarefied Slit Flows—Part I: DSMC Simulation," *Physics of Fluids A*, Vol. 5, No. 1, 1993, pp. 235–242.

[19]Wadsworth, D. C., and Erwin, D. A., "Numerical Analysis of Rarefied Slit Flows, Part II: Navier–Stokes Results," AIAA Paper 91-1748, June 1991.

[20]Nadiga, B. T., "An Euler Solver Based on Locally Adaptive Discrete Velocities," *Journal of Statistical Physics*, Vol. 81, No. 1-2, 1995, pp. 129–146.

[21]Nadiga, B. T., "An Adaptive Discrete Velocity Model for the Shallow Water Wave Equations," *Journal of Computational Physics*, Vol. 121, No. 2, 1995, pp. 271–280.

[22]Nadiga, B. T., and Pullin, D. I., "A Method for Near-Equilibrium Discrete-Velocity Gas Flows," *Journal of Computational Physics*, Vol. 112, No. 1, 1994, pp. 162–172.

[23]Ivanov, M. S., and Rogasinsky, S. V., "Theoretical Analysis of Traditional and Modern Schemes of the DSMC Method," *Rarefied Gas Dynamics: Proceedings of the 17th International Symposium on Rarefied Gas Dynamics*, edited by A. E. Beylich, VCH Verlagsgesellschaft mbH, Weinheim, Germany, 1991, pp. 629–642.

[24]Gimelshein, S. F., and Ivanov, M. S., "Investigation of Shock Wave Structures by Majorant Cell and Free Cell Schemes of DSMC," *Rarefied Gas Dynamics: Proceedings of the 17th International Symposium on Rarefied Gas Dynamics*, edited by A. E. Beylich, VCH Verlagsgesellschaft mbH, Weinheim, Germany, 1991, pp. 718–726.

[25]Boyd, I. D., Chen, G., and Candler, G. V., "Predicting the Failure of the Continuum Fluid Equations in Transitional Hypersonic Flows," AIAA Paper 94-2352, June 1994.

[26]Bird, G. A., "Breakdown of Translational and Rotational Equilibrium in Gaseous Expansion," *AIAA Journal*, Vol. 8, No. 11, 1970, pp. 1998–2003.

[27]Liepmann, H. W., and Roshko, A., *Elements of Gas Dynamics*, Wiley, New York, 1957, pp. 53, 54.

R. G. Wilmoth
Associate Editor